

Picocavity modal analysis: A multiple-scattering approach for picoscopic mode coupling

Saeid Asgarnezhad-Zorgabad ^{1,*}, Jeremy J. Baumberg ^{2,†} and Ortwin Hess ^{1,3,‡}

¹*School of Physics and CRANN Institute, Trinity College Dublin, University of Dublin, Dublin 2, D02 PN40, Ireland*

²*NanoPhotonics Centre, Cavendish Laboratory, Department of Physics, University of Cambridge, Cambridge CB3 0HE, United Kingdom*

³*AMBER, SFI Research Centre for Advanced Materials and BioEngineering Research, Trinity College Dublin, University of Dublin, Dublin 2, D02 PN40, Ireland*



(Received 11 December 2023; accepted 15 December 2024; published 7 January 2025)

Picocavities serve as exceptional platforms for extreme atomic-scale field localization, enabling opportunities for light-matter interactions at subnanometer scales. Here we introduce a scattering-theory-based mode analysis approach to model the interaction between picocavity and nanocavity modes, providing insights into picoscopic field-field dynamics. By employing coupled-mode theory, we specifically investigate the coupling between multiple nanocavity quasinormal modes (QNMs) and a single picocavity QNM, highlighting the development of spectral correlations through mode hybridization. Our findings reveal that the induced hybridization can be controlled by adjusting the picocavity geometry and the frequency spacing of the excited modes. This strong field-field coupling at picoscopic scales leads to spectral mixing, which alters the optical density of states, facilitates the identification of Fano resonances, and produces spectrally stable picocavity modes with modified mode-mixing characteristics. Furthermore, the coupled-mode framework enables the modeling of quantum dynamics resembling the Jaynes-Cummings model, describing the interaction between a hybridized two-level system and a quantized picocavity field. These insights into picoscopic light-matter interactions pave the way for advancements in subnanometer photonic quantum dynamics.

DOI: [10.1103/PhysRevResearch.7.013026](https://doi.org/10.1103/PhysRevResearch.7.013026)

I. INTRODUCTION

Picocavities, which confine light at the atomic scale, can form within tightly confined plasmonic nanocavities, such as the nanoparticle-on-mirror (NPOM) structure, through mechanisms like a single gold atom protrusion. In this picocavity-inside-NPOM configuration [1–4], the gold atom is drawn out by light and stabilized via the polarizability of a nearby tip atom, remaining attached to the nanoparticle surface through coordination bonding. This adatom remains stable for several minutes at room temperature and significantly longer at cryogenic temperatures [4]. With an optical mode volume of 1 nm^3 or less, picocavities are crucial for applications including single-molecule optomechanics [3], ultrafast polaritonic interactions [5], optical spring effects [2], and many others [1,2,4].

The quantitative analysis of the picocavity-inside-NPOM configuration, including its electromagnetic-field dynamics and interaction with a quantum emitter, presents three major challenges in nano- and picophotonics [1–11]: (i) accurately

calculating the electromagnetic field within the NPOM geometry [6–8], (ii) modeling a single or a few gold atoms as subnanometer metallic entities on the NPOM surface (see, e.g., Ref. [4]), and (iii) understanding the dynamics of a dipolar emitter in proximity to a nanostructure [9–11]. Addressing these challenges, the near-field properties of the picocavity-inside-NPOM architecture have been explored through various theoretical and numerical methods, including finite-difference time-domain simulations [12], quantum density-functional theory [13], and dipole approximations [4]. While these approaches have yielded valuable insights, recent experiments [2] on picoscopic optomechanical phenomena underscore the need for a more comprehensive yet intuitive framework, particularly one that captures mode coupling and picoscopic field evolution.

Building on earlier studies, this work focuses on two key unresolved questions. First, can a theoretical framework based on a multiscattering formalism be developed to analyze the evolution of light within a picocavity-inside-NPOM system? Second, is it possible to quantize these leaky modes and establish a robust theoretical basis for describing the quantum interaction between atomically confined light and a two-level quantum emitter?

Recent studies have established mode coupling between nanocavity and picocavity quasinormal modes (QNMs) through approaches such as incorporating nonclassical corrections into a quantum hydrodynamic model linked with QNM theory [14] or utilizing fully vectorial computations with surface-response quantum corrections [15]. Here we introduce a theoretical formalism that models the picocavity and

*Contact author: sasgarnezhad93@gmail.com

†Contact author: jjb12@cam.ac.uk

‡Contact author: ortwin.hess@tcd.ie

nanocavity as two displaced scatterers with distinct shapes, each characterized by its own QNMs. The resulting coupled-mode equations (4) extend traditional coupled-mode theory [16–18], by incorporating self- and cross-coupling coefficients specific to nano- and picocavity QNMs. This framework thus complements existing research and addresses the challenges (i)–(iii) previously outlined in nano- and picophotonics but differs fundamentally by employing a bi-object scattering approach. This novel perspective facilitates a quantum description of the interaction between the picocavity and a two-level quantum emitter, enhancing our understanding of field-field and field-matter interactions at picoscopic scales. Notably, we demonstrate the utility of this formalism by analyzing the interaction between the quantized picocavity mode and a two-level quantum emitter, effectively capturing the dynamics of the picoscopic light-matter interaction.

II. MODEL

We consider a metal nanoparticle with a facet width w placed just above a planar gold surface forming an NPOM with a gap size $d \sim 1$ nm. At the center of the nanofacet, we assume a single (or a few) gold atom(s) with a scalable protrusion, which we consider to have optical properties given by the permittivity of bulk gold $\varepsilon_m = \varepsilon_{m,r} + i\varepsilon_{m,i}$ as this seems to confirm (along with time-dependent density-functional-theory calculations) vibrational nonlinear spectroscopy experiments [3,12]. This protuberance has volume V and semiaxes a_j , $j \in x, y, z$, with z the axis perpendicular to the nanofacet. Here we set $a_x = a_y = 0.15$ nm and $a_z = \phi a_{x,y}$ for $\phi = a_z/a_{x,y}$ the aspect ratio. Following previous studies [13,15], we consider ϕ as a control parameter of the picocavity geometry, achieved by pulling a few adatoms different distances out of the Au surface. This forms a stacked configuration that we approximate with a half ellipsoid. For simplicity, our minimal model disregards explicit information about, for example, the electronic structure and materials-related quantum features such as charge transfer between the NPOM structure and nearby emitter. Here, to model half-oblate ellipsoid, we assume $a_z > a_{x,y}$, define $e = \sqrt{1 - \phi^{-2}}$ to give $L_z(\phi) = e^{-3}(1 - e^2)(\tanh^{-1} e - e)$, and assume a multiplicative structural factor

$$L_s(\omega) = 1 - \mathcal{N} \frac{\varepsilon_m(\omega) - \varepsilon_g}{\varepsilon_m(\omega) + \varepsilon_g},$$

with $\mathcal{N} = 0.19$.¹ Finally, by defining $f(\omega) = [1 - \varepsilon_m(\omega)/\varepsilon_g]^{-1}$ as the spectral parameter, we express the polarizability as [4,19]

$$\tilde{\alpha}_z(\omega, \phi) := \frac{\alpha(\omega, \phi)}{\varepsilon_0 V} = \frac{1}{L_z(\phi)L_s(\omega) - f(\omega)}. \quad (1)$$

¹Indeed, polarizability of a half ellipsoid is achievable either by using theoretical methods such as spectral representation [19] or a solution to the Laplace equation (see Appendix A) or by using numerical methods such as finite-difference time-domain [12] or quantum hydrodynamic correction to QNM theory [14,15]. We fix $\mathcal{N} = 0.19$ to match the theory with numerical calculations.

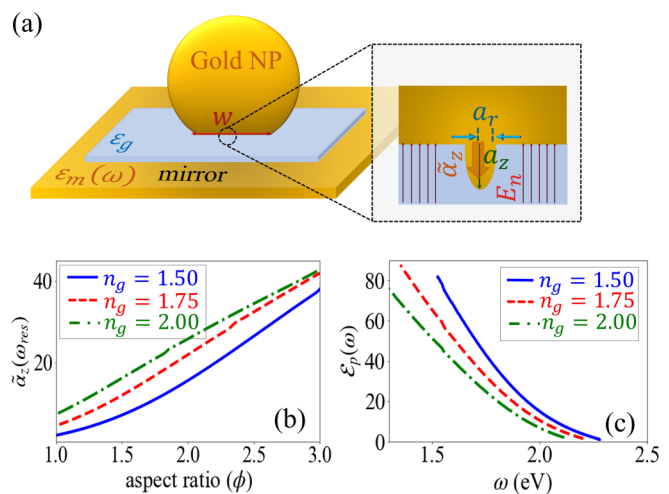


FIG. 1. (a) NPOM configuration with $2R = 80$ nm, width $w = 10$ nm, gap size $d = 1$ nm, and atomic protrusion below the flat gold nanoparticle facet. The nanoparticle has permittivity $\varepsilon_m(\omega)$ and also has nanogap material of refractive index $n_g = \sqrt{\varepsilon_g}$ supporting the electric-field amplitude E_n . The inset shows a protrusion of radius a_j , $j \in \{r, z\}$, for polarizability $\tilde{\alpha}_z$. (b) Polarizability of picocavity resonance vs ϕ for various n_g . (c) Maximum field enhancement $\mathcal{E}_p(\omega) = |E_p/E_n|$ for various n_g .

We note that Eq. (1) can also be obtained by analyzing the scalar potential. In Appendix A we present quantitative steps towards the derivation of the polarizability for the picocavity-inside-NPOM configuration [namely, Eq. (1)], based on the spherical harmonic representation of the nanocavity QNMs and utilizing the solution of Laplace equation [6]. Characterizing $\tilde{\alpha}_z(\omega, \phi)$, we determine $f(\omega)$ and $L_s(\omega)$ by fitting $\varepsilon_m(\omega)$ to the optical dielectric function of gold [20] and pick up the picocavity resonances by numerically finding (1) as $\tilde{\alpha}_z(\omega_{\text{res}}) = \max[\tilde{\alpha}_z(\omega, \phi)]$, for various $\phi \in [1, 3]$ in Fig. 1(b).

Emission properties. To determine the emission properties, we assume that the size of the picocavity is much smaller than the nanocavity facet and also is small compared to the gap size, allowing us to approximate the picocavity field reradiation as dipole radiation emitted by a polarized nanoparticle. Hence, the picocavity effectively experiences a uniformly distributed nanocavity field E_n inducing the polarizability $\tilde{\alpha}_z(\omega, \phi)$ [4]. We then define the effective dipole $\mathbf{p}(\omega, \phi) = \tilde{\alpha}_z(\omega, \phi)\mathbf{E}_n$ and exploit the superposition principle to obtain for the picocavity $\mathbf{E}_p(r, \omega, \phi) = \mathbf{E}_n + \{[\mathbf{p}(\omega, \phi) \cdot \hat{\mathbf{r}}]\hat{\mathbf{r}} - \mathbf{p}(\omega, \phi)\}/4\pi\varepsilon_0 r^3$, with $\hat{\mathbf{r}}$ the unit vector along \mathbf{r} . For specificity, we set $|\mathbf{r}_0| = 0.1$ nm and find $\max[|\mathbf{E}_p(\mathbf{r}_0, \omega, \phi)|]$ for $\phi \in [1, 3]$ to retrieve a maximum field enhancement factor $\mathcal{E}_p(\omega) = |E_p/E_n|$ as shown in Fig. 1(c). This results in field enhancements up to tenfold larger than in the NPOM nanocavities and similarly high polarizabilities. Reflecting extreme field localization and enhancements [Figs. 1(b) and 1(c)] show the characteristic spectral features of the picocavity field, allowing us to consider the picocavity and the nanocavity as two distinct linear scatterers. We note that while our simple dipole-field approximation of the picocavity reradiation may be suitable for the picocavity mode analysis here, it cannot be used for an optically measured spectrum as it disregards effects such as quadruple fields [21,22].

III. THEORY

Here we aim to provide detailed quantitative and qualitative steps toward a multiscattering framework for the picocavity-inside-NPOM configuration to exploit it for exploring picocavity mode evolution and quantization. Since our scheme resembles a cavity-inside-nanocavity architecture, we should follow three quantitative steps required for cavity field quantization: (i) coupling input to output ports via the cavity configuration (input-output theory), (ii) modal evolution of the cavity via coupled-mode theory, and (iii) field quantization of the excited mode(s). Here we first establish a biobject scattering framework for the picocavity-inside-NPOM scheme in Sec. III A and derive the generalized coupled-mode theory in Sec. III B. We then exploit this formalism to characterize the modal evolution and hybridization of the picocavity, calculate its field quantization, and investigate the coupling of the quantized picocavity field to the resonant two-level quantum emitter in Sec. V.

A. Biobject scattering formalism for picocavity-inside-NPOM configuration

We treat the NPOM and picocavity as two differently shaped biscattering objects, use complex linear scattering, and exploit input-output theory [23] to describe its scattering properties. Specifically, the NPOM (picocavity) has N_n (N_p) resonances that may couple to an incoming wave through N_{sc} different ports. Qualitatively, scattering modes and input-output waves couple through two ways: (i) incoming and outgoing modes via the eigenmodes of the scatterers at the input and output ports (termed propagating modes) and (ii) direct incoming to outgoing modes. These incoming and outgoing modes do not play a role in constructing scatterer modes but are necessary to set up an input-output theory. Assuming that the m th propagating mode is associated with the wave vector $\mathbf{k}_m(\omega)$ and spatial distribution $\mathbf{s}_m(\mathbf{r}, \omega)$, we define $\mathbf{r}_m = \mathbf{r}_m^{\parallel} + \mathbf{r}_m^{\perp}$ for \mathbf{r}_m^{\parallel} the propagation and $\mathbf{r}_m^{\perp} \perp \mathbf{k}_m(\omega)$ the transverse direction, as the position of the m th coupling port. Then the transverse field part $\mathbf{s}_m = \mathbf{s}_m^{\perp}(\mathbf{r}_m^{\perp}, \omega)e^{ik_m r_m^{\parallel}}$ carries power to the scatterers. As they propagate outside the scatterer in a lossless dielectric, we consider $\langle \mathbf{s}_m^{\perp} | \mathbf{s}_n^{\perp} \rangle = \delta_{mn}$ as the orthogonality condition. Then we can underpin coupled-mode theory based on these input-output assumptions. Here we assume that the picocavity is a pointlike scatterer, for which multiple scattering is negligible, and that the superposition principle is applicable for scattered field calculations [24], which justifies our assumption of distinct biobject scatterers, thus considering separate treatments of the NPOM (without picocavity) and picocavity (without NPOM).

To set up an input-output theory for the picocavity-inside-nanocavity system we must use a complete set of modes for the picocavity and the NPOM modes and fix boundary conditions that provide well-defined picocavity and/or nanocavity fields. Specifically, we choose classical QNMs for both the NPOM and the picocavity as a possible complete set to test the applicability of multiscattering theory for picoscopic modal analysis. We emphasize that for gaps less than or equal to 1 nm, nonclassical effects are relevant and classical electromagnetic theory is insufficient to capture the full dynamics.

Hence, subsequently extending our assumptions, using non-classical electromagnetic theory as developed, for example, in Refs. [25–29], should provide better accuracy. The present work focuses on developing the scattering formalism, hence including nonclassical corrections is beyond its current scope.

As we show in Sec. II, our assumption of modeling the picocavity-inside-NPOM system as an elongated ellipsoidal nanoparticle and using classical QNMs provides equivalent (but not fully accurate) near-field features compared to non-classical QNMs [14,15]. Following classical QNM theory [30], we consider position-dependent effective-mode volumes for the picocavity (p) and nanocavity (n) as $V_{\text{eff}}^{(i)}(\mathbf{r}_0')$ (which hereafter we abbreviate as $V_{\text{eff}}^{(i)}$), with $i \in \{n, p\}$, assume the l th picocavity (nanocavity) QNMs as $\tilde{\mathbf{E}}_l^{(p)}(\mathbf{r})$ [$\tilde{\mathbf{E}}_l^{(n)}(\mathbf{r})$] satisfying classical QNM algebra, and define $\tilde{\omega}_{pl}$ ($\tilde{\omega}_{nl}$) as their corresponding eigenfrequencies [16]. Specifically, we express the nanocavity field comprising N_n modes using coefficients $a_l(\omega)$ as $\boldsymbol{\psi}^{(n)}(\mathbf{r}, \omega) = \sum_{l=1}^{N_n} a_l(\omega) \tilde{\mathbf{E}}_l^{(n)}(\mathbf{r})$ [31] and also use $b_l(\omega)$ coefficients to describe the picocavity field including N_p modes as $\boldsymbol{\psi}^{(p)}(\mathbf{r}, \omega) = \sum_{l=1}^{N_p} b_l(\omega) \tilde{\mathbf{E}}_l^{(p)}(\mathbf{r})$.

Building on the traditional electromagnetic scattering formalism [32], the fields evolving within the picocavity-inside-NPOM configuration must satisfy two sets of scattering boundary conditions. The first pertains to the continuity of the displacement field vector, which applies to any metal-dielectric surface with zero external charge density. The second involves conditions dictated by the algebra of QNMs. To define the scattering boundary associated with the displacement field vector and the continuity of the scalar potential, we adopt the approach detailed in Ref. [6]. Specifically, we enforce a zero scalar potential at the surfaces of both the nanoparticle facet and the picocavity, while ensuring continuity in the normal component of the electric displacement vector (see Appendix A for the mathematical formulation).

However, it is important to note that the theoretical framework in Ref. [6] relies on spherical harmonics, which form a complete orthogonal set of modes. The orthogonality relation for these modes, given in Eq. (A9), differs significantly from the orthogonality relation for our nanocavity QNMs, as described in Eq. (A10). Consequently, our formalism requires an additional boundary condition to incorporate the QNM algebra. Specifically, for nanocavity and picocavity QNMs, we assume that the effective potential $V_{\text{eff}}^{(p)}$ is the same for all picocavity QNMs introducing a bounding surface at $\mathbf{r} = \mathbf{r}_0$, which encloses the geometrical volume $V(\mathbf{r}_0)$.

The picocavity-inside-nanocavity system then acts as a composite scatterer, including fields related to both scatterers, which for well-defined fields provides field-field coupling inside picoscopic volumes $V(\mathbf{r}_0)$. Quantitatively, we express the scattered field $\boldsymbol{\psi}_{sc}(\mathbf{r}, \omega)$ inside $V(\mathbf{r}_0)$ using classical QNMs. However, in-between the picocavity and NPOM volumes $V_{np} = V(\mathbf{r}_0^{\text{n}}) - V(\mathbf{r}_0)$, $\mathbf{r} \in V_{np}$, for \mathbf{r}_0^{n} the surface that included nanocavity QNMs, we assume that the picocavity-inside-NPOM system possesses N_{sc} coupling ports. Then the scattered field $\boldsymbol{\psi}_{sc}(\mathbf{r}, \omega)$ includes nanocavity QNMs, a complete set of N_{sc} incoming propagating modes, each of which has an amplitude \mathcal{S}_{sc}^i , and a weak evanescent field $\boldsymbol{\psi}_{\text{ev}}^{(p)}(\mathbf{r}, \omega)$ which directly propagates inside $V(\mathbf{r}_0)$. We assume that picocavity or nanocavity QNMs interact with $\boldsymbol{\psi}_{sc}(\mathbf{r}, \omega)$ through

coupling ports, but $\psi_{\text{ev}}^{(\text{p})}(\mathbf{r}, \omega)$ interact only with nanocavity QNMs. For the scattered field due to propagating modes, we have $\psi_{\text{sc}}^{(\text{p})} = \sum_{j=1}^{N_{\text{sc}}} \mathcal{S}_{\text{sc}}^j s_j^{\perp}(\mathbf{r}^{\perp}, \omega) \exp(i\Theta_j^{\text{p}}) + \psi_{\text{ev}}^{(\text{p})}(\mathbf{r}, \omega)$, where $\Theta_j^{\text{p}} = k_j(r_j^{\parallel} - r_j^{\parallel})$ (for $\mathbf{r}_j = \mathbf{r}_j^{\perp} + r_j^{\parallel}$ the position of j th port) represents the oscillatory phase along the propagation direction. Then we express the scattered field as

$$\psi_{\text{sc}}(\mathbf{r}, \omega) = \begin{cases} \psi^{(\text{n})}(\mathbf{r}, \omega) + \psi^{(\text{p})}(\mathbf{r}, \omega), & \mathbf{r} \in V(\mathbf{r}_0) \\ \psi^{(\text{n})}(\mathbf{r}, \omega) + \psi_{\text{sc}}^{(\text{p})}, & \mathbf{r} \in V_{\text{np}}. \end{cases} \quad (2)$$

Mode matching at $\mathbf{r} = \mathbf{r}_0$ yields $\mathcal{S}_{\text{sc}}^j = \exp[-ik_j(r_0^{\parallel} - r_j^{\parallel})] \sum_{l=1}^{N_{\text{p}}} s_j^{\perp*}(\mathbf{r}^{\perp}, \omega) \cdot \tilde{\mathbf{E}}_l^{(\text{p})}(\mathbf{r}_0) b_l(\omega)$, which couples the input power to picocavity QNMs. Following these considerations, for $\mathbf{r} \in V(\mathbf{r}_0)$ we assume $\psi_{\text{sc}}^{(\text{p})} := \psi_{\text{inc}} = \psi_{\text{inc}}^{(\text{p})} + \psi_{\text{ev}}^{(\text{p})}(\mathbf{r}, \omega)$ and assume it as an incoming wave ψ_{inc} [here taken as a probe TM plane wave with $|\psi_{\text{inc}}| = 1$ V/m and with small polar angle satisfying $\cos(\theta) \approx 1$]. For our region of interest $V(\mathbf{r}_0)$, picocavity QNMs satisfy both orthogonality and normalization conditions, while nanocavity QNMs satisfy only the orthogonality condition, providing well-defined fields for picocavity mode analysis.

B. Generalized quasinormal coupled-mode theory for picocavity-inside-NPOM structures

We now investigate the dynamics of the picocavity mode for $\mathbf{r} \in V(\mathbf{r}_0)$ through an analysis of the total field $\psi(\mathbf{r}, \omega) = \psi_{\text{inc}} + \psi_{\text{sc}}(\mathbf{r}, \omega)$. Here we employ Maxwell's equations, primarily $\nabla \times \psi(\mathbf{r}, \omega) = i\omega \varepsilon(\mathbf{r}, \omega) \psi(\mathbf{r}, \omega)$, where $\varepsilon(\mathbf{r}, \omega) = \varepsilon_{\text{BG}} + \Delta\varepsilon(\mathbf{r}, \omega)$, ε_{BG} is the permittivity of the nanogap material, and $\Delta\varepsilon(\mathbf{r}, \omega)$ is the local permittivity in which the picocavity is embedded. Utilizing the equivalent equation for ψ_{inc} , $\nabla \times \psi_{\text{inc}} = i\omega \varepsilon_{\text{BG}} \psi_{\text{inc}}$, we derive the scattered field evolution as

$$\nabla \times \psi_{\text{sc}}(\mathbf{r}, \omega) - i\omega \varepsilon(\mathbf{r}, \omega) \psi_{\text{sc}}(\mathbf{r}, \omega) = i\omega \Delta\varepsilon(\mathbf{r}, \omega) \psi_{\text{inc}}. \quad (3)$$

We then find the subsequent field evolution through several quantitative steps, specifically by plugging (2) into (3), and then use the QNM definition and orthogonality conditions [30,33].

Next, for an appraisal of the picoscopic coupled-mode formalism, we define, for the n th and m th picocavity or nanocavity QNMs, the nanocavity (picocavity) normalization coefficients as

$$\mathcal{N}_{nm}^{(\text{n})} = \int_{V_{\text{eff}}^{(\text{p})}} d^3 \mathbf{r}' \tilde{\mathbf{E}}_n^{*(\text{n})}(\mathbf{r}') \partial_{\omega} [\omega \varepsilon(\omega)]_{\omega=\tilde{\omega}_m^{(\text{n})}} \tilde{\mathbf{E}}_m^{(\text{n})}(\mathbf{r}')$$

and overlap coefficients between picocavity and nanocavity QNMs as

$$\mathcal{K}_{nm}^{(\text{n})} = \int_{V_{\text{eff}}^{(\text{p})}} d^3 \mathbf{r}' \tilde{\mathbf{E}}_n^{*(\text{n})}(\mathbf{r}') \partial_{\omega} [\omega \varepsilon(\omega)]_{\omega=\tilde{\omega}_m^{(\text{p})}} \tilde{\mathbf{E}}_m^{(\text{p})}(\mathbf{r}'),$$

$$\mathcal{K}_{nm}^{(\text{p})} = \int_{V_{\text{eff}}^{(\text{p})}} d^3 \mathbf{r}' \tilde{\mathbf{E}}_n^{*(\text{p})}(\mathbf{r}') \partial_{\omega} [\omega \varepsilon(\omega)]_{\omega=\tilde{\omega}_m^{(\text{n})}} \tilde{\mathbf{E}}_m^{(\text{n})}(\mathbf{r}').$$

We further assume that the coupling picocavity and nanocavity QNMs to ψ_{inc} are different and define $\mathcal{I}^{(\text{t})} = \int d^3 \mathbf{r}' \tilde{\mathbf{E}}_n^{*(\text{t})}(\mathbf{r}') \cdot \Delta\varepsilon(\mathbf{r}', \omega) \psi_{\text{inc}}$ representing their coupling.

Then we obtain the generalized coupled-mode theory as

$$\begin{aligned} \mathcal{N}^{(\text{n})}(\mathcal{W}^{(\text{n})} - \omega) \mathbf{a}(\omega) + \mathcal{K}^{(\text{n})}(\mathcal{W}^{(\text{p})} - \omega) \mathbf{b}(\omega) &= \omega \mathcal{I}^{(\text{n})}, \\ \mathcal{N}^{(\text{p})}(\mathcal{W}^{(\text{p})} - \omega) \mathbf{b}(\omega) + \mathcal{K}^{(\text{p})}(\mathcal{W}^{(\text{n})} - \omega) \mathbf{a}(\omega) &= \omega \mathcal{I}^{(\text{p})}, \end{aligned} \quad (4)$$

where $\mathcal{W}^{(\text{t})} = \text{diag}(\tilde{\omega}_{t1}, \dots)$ defines the picocavity or nanocavity eigenfrequencies. We note that due to the integration over $V(\mathbf{r}_0)$, $\mathcal{N}^{(\text{p})}$ can resemble a δ distribution. However, as the nanocavity QNM normalization is only provided for $V(\mathbf{r}_0^{\text{n}})$, $\mathcal{N}^{(\text{n})}$ differs from a δ distribution. We note further that (4) differs from traditional QNM coupled-mode theory [17,18] for which incorporating QNMs to input-output formalism, without specifying scattering boundaries, always yields a coupled-mode equation. In our case, the modes are confined by the scattering boundary, for which nanocavity and picocavity QNMs become well defined (picocavity QNMs are orthonormal, but nanocavity QNMs are orthogonal but not normalized); thus (4) exhibits different cross-coupling $\mathcal{K}^{(\text{t})}$ and normalization (self-coupling) $\mathcal{N}^{(\text{t})}$ coefficients.

IV. PICOCAVITY MODAL ANALYSIS

We point out that the picocavity mode is spectrally broad to cover all nanocavity modes yielding mode hybridization between picocavity and nanocavity QNMs. Here we use (4) to realize this hybridization among broad picocavity QNMs at frequency $\tilde{\omega}_{\text{p}}(\phi)$ and multiple nanocavity frequencies $(\tilde{\omega}_{\text{n1}}, \tilde{\omega}_{\text{n2}}, \dots)$, which we found using methods developed in Ref. [31]. These nanocavity modes encompass spatially symmetric and asymmetric modes inside $V_{\text{eff}}^{(\text{p})}$. Modes exhibiting significant overlap with the picocavity field hybridize and thereby contribute to the picoscopic mode evolution. By carefully calculating the overlap integrals in (4), we identify only two nanocavity modes $\tilde{\omega}_{\text{n1}} \approx 2.07$ eV and $\tilde{\omega}_{\text{n2}} \approx 2.18$ eV, corresponding to bright (symmetric circular distribution) and dark nanocavity (antisymmetric spatial distribution with odd parity) modes, respectively, which interact with broad $\tilde{\omega}_{\text{p}}(\phi)$ (spatially distributed as a dipole radiation pattern) (see Appendix B for further details). Three hybridized modes (high-, middle-, and low-energy branches) emerge from this interaction [Figs. 2(a) and 3(a)].

Interestingly, mode hybridization in our scheme reveals the interaction of the system with discrete and continuous spectra.² Indeed, picocavity and nanocavity resonances are complex eigenfrequencies corresponding to the poles of the scattering matrix, and ϕ acts as a continuous parameter that realizes the interaction among continuous (picocavity) and a few discrete (nanocavity) eigenfrequencies, justifying that Fig. 2(a) represents the interaction between a continuous picocavity mode $\tilde{\omega}_{\text{p}}$ and a few discrete nanocavity modes $\tilde{\omega}_{\text{n}}$. Here the blueshifted mode $\tilde{\omega}_{+}$ [dark blue in Fig. 2(a)] corresponds to the picocavity mode for small aspect ratios $\phi \ll 1$ (labeled Geo. 1), becoming the $\tilde{\omega}_{\text{n2}}$ nanocavity mode for $\phi = 2.5$ (Geo. 3). An intermediate mode ω_0 [violet solid line in Fig. 2(a)] interconnects two nanocavity modes, while the dark red line

²A similar problem has been considered in quantum mechanics; see, e.g., Ref. [34].

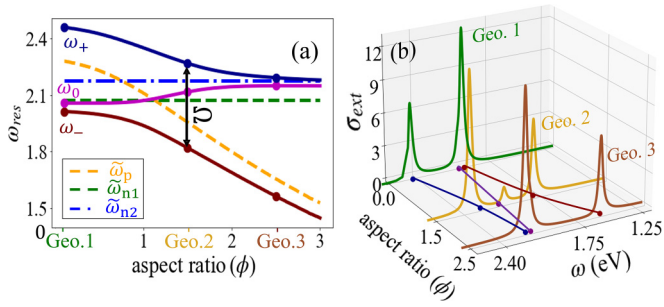


FIG. 2. Mode hybridization based on coupled-mode theory. (a) Original picocavity (orange dashed line) and nanocavity (green dashed and blue dash-dotted lines) modes for three different geometries (labeled “Geo.”). Dark blue ω_+ , violet ω_0 , and maroon solid curves ω_- denote the mixed modes from picocavity-nanocavity mode hybridization. For Geo. 2, an enhancement of the normal-mode splitting up to $\Omega = 350$ meV is achieved. (b) Evolution of the extinction coefficient for three different geometries. We assume $r_0^{(s)} = 0.1$ nm from the gold adatom.

ω_- redshifts from $\tilde{\omega}_{n1}$ at $\phi \ll 1$ but evolves into the picocavity mode by $\phi = 2.5$.

The appearance of the ω_0 branch holds particular significance as it unveils two previously unexplored aspects of picoscopic field interactions. First, it demonstrates mixing between dark and bright modes ($\tilde{\omega}_{n1, n2}$) due to their coupling to $\tilde{\omega}_p(\phi)$. This is seen with the trajectory of the violet solid line in Fig. 2(a). Second, this mode also amplifies the mode splitting of $\Omega \approx 350$ meV between ω_+ and ω_- at $\phi = 1.5$, predicting

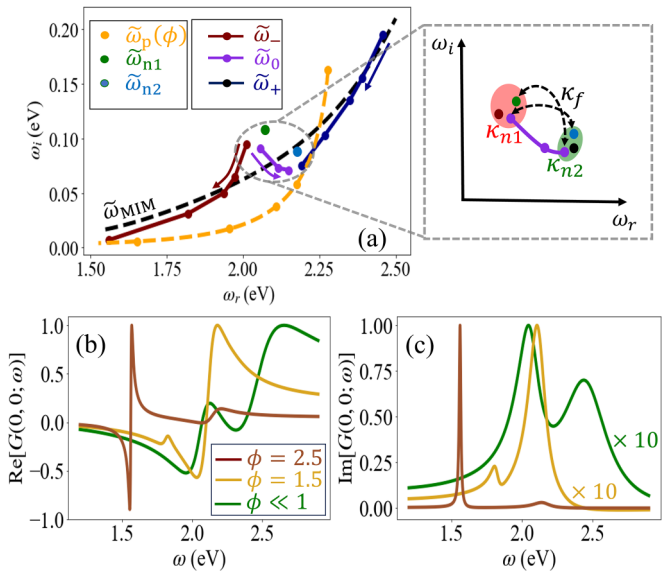


FIG. 3. (a) Hybridized mode evolution in the complex $\tilde{\Omega} = \omega_r + i\omega_i$ plane. Arrows show the evolution of hybridized eigenfrequency for increasing ϕ . The infinite metal-insulator-metal eigenfrequency approximation is shown by the black dashed line. The inset represents the details of mode mixing: red and green shaded ellipses represent allowed mixed modes, while κ_f represents inaccessible mode mixing. (b) Real and (c) imaginary parts of the reconstructed Green’s function for three cases: small $\phi \ll 1$, $\phi = 1.5$, and sharp $\phi = 2.5$ protrusions.

strong mode coupling through mode hybridization [seen for Geo. 2 in Figs. 2(a) and 2(b)]. To gain a deeper understanding of the strong intermode coupling in Geo. 2, we calculate the extinction response using the optical theorem that relates \mathbf{E}_{inc} to scattered field \mathbf{E}_{sc} in a medium surrounded by wave number k_g through $\sigma_{\text{ext}}(\omega, \phi) = 4\pi \text{Im}(\mathbf{E}_{\text{inc}}^* \cdot \mathbf{E}_{\text{sc}}) / k_g |\mathbf{E}_{\text{inc}}|^2$. We express scattered fields in terms of eigenfunctions of the hybridized system $\mathbf{E}_{\text{sc}} = \sum_J \mathbf{E}_J(\mathbf{r}, \omega)$, $J \in \{-, 0, +\}$, decomposable as $\mathbf{E}_J(\mathbf{r}_0^{(s)}, \omega) = \mathcal{A}_J(\omega) \mathbf{E}_J(\mathbf{r}_0^{(s)})$, with $r_0^{(s)} < r_0$ a position inside the effective mode volume (fixed for calculating the scattered field). Inserting this into the optical theorem, using $\mathbf{E}_{\text{inc}}^* \cdot \mathbf{E}_{\text{sc}} = |\mathbf{E}_{\text{inc}}^*| |\mathbf{E}_{\text{sc}}|$, and neglecting the resultant coefficient, we obtain the excitation response within the picocavity mode volume as

$$\sigma_{\text{ext}}(\omega, \phi) = \sum_J \mathcal{A}_J(\omega) E_J(\mathbf{r}_0^{(s)}), \quad (5)$$

where $\mathcal{A}_J(\omega) = \text{Im}[(\omega_J^2 - \omega^2 + 2i\gamma_J\omega)^{-1}]$ is the spectral function of hybridized QNMs and $\tilde{\omega}_J = \omega_J + i\gamma_J$. We observe a double-peak spectrum for limiting cases of $\phi \ll 1$ (Geo. 1) and $\phi = 2.5$ (Geo. 3) due to the dominant contributions of ω_+ and ω_- [green and brown solid lines in Fig. 2(b)]. However, for $\phi = 1.5$, the ω_0 mode contribution becomes significant due to enhanced normal-mode splitting and is seen as a third peak in the system resonance [yellow solid line in Fig. 2(b)]. We refer to this as strong intermode coupling at the picoscopic scale and is a generalization of strong field-field interactions originally proposed in Ref. [15].

This modal analysis of the hybridized fields for various ϕ gives detailed insights into the behavior of the complex spectral frequencies with real and imaginary parts ω_r and ω_i , respectively. Let us consider $w = 10$ nm and investigate the spectral correlations between hybridized modes. For $\phi \ll 1$, the eigenfrequencies begin to evolve with $\tilde{\omega}_+ = 2.46 + 0.195i$ eV, $\tilde{\omega}_0 = 2.05 + 0.091i$ eV, and $\tilde{\omega}_- = 2.01 + 0.095i$ eV. Here $\tilde{\omega}_p$ is spectrally closer to $\tilde{\omega}_{n2}$ than $\tilde{\omega}_{n1}$, yielding considerable overlap between $\tilde{\omega}_p$ and $\tilde{\omega}_{n2}$, while overlap between $\tilde{\omega}_p$ and $\tilde{\omega}_{n1}$ is forbidden. Then the mode $\tilde{\omega}_{n2}$ exhibits a bifurcation due to hybridization with $\tilde{\omega}_p$ [Figs. 2(a) and 3(a)]. This bifurcation enhances as ϕ increases, giving blueshifts of $\tilde{\omega}_0$ and redshifts of $\tilde{\omega}_-$ and $\tilde{\omega}_+$ branches. While $\tilde{\omega}_0$ and $\tilde{\omega}_+$ branches converge asymptotically to $\tilde{\omega}_{n2}$, we find that ω_+ transforms into a stable picocavity mode for $\phi = 2.5$, as indicated by the arrows in Fig. 3(a).

On the basis of our pico- and nanocavity mode analysis, larger aspect ratios lead to resonances with lower frequencies [orange dashed line in Fig. 2(a)] and lower dissipation [orange dashed line in Fig. 3(a)]. This can be qualitatively explained in terms of Fabry-Pérot resonances [35]. The picocavity (which extends from the nanoparticle) facet can be approximated as a terminated facet with modulus of reflectivity $r \sim 1$, while the picocavity tip acts as an ellipsoidal termination (resembling a half-ellipsoidal Fabry-Pérot resonator). In this qualitative geometry, reflection is complex, and the phase related to this reflection affects the Fabry-Pérot resonance condition, i.e., the total accumulated phase of a plasmon wave in one round-trip (l_r) should be an integer multiple of 2π . A higher round-trip phase, at larger aspect ratios, leads to a phase accumulation proportional to $\text{Re}(\tilde{\omega}l_r/c)$, where $\tilde{\omega}$ is the

Fabry-Pérot resonance. This clearly shows that the picocavity resonances decrease as the aspect ratio increases. The weak dissipation for this resonance reflects the minimum of the dissipation of crystalline gold [20].

The interdependence between hybrid modes is influenced by the frequency separation between original modes. Larger ω_r leads to reduced overlap between the picocavity and nanocavity fields, with mixing only for small frequency separation. Specifically, for $\phi \ll 1$, ω_0 and ω_- are spectrally close and $\int d^3r \tilde{\mathbf{E}}^{*(p)} \cdot \tilde{\mathbf{E}}_1^{(n)} \gg \int d^3r \tilde{\mathbf{E}}^{*(p)} \cdot \tilde{\mathbf{E}}_2^{(n)}$; consequently, these modes are hybridized, while for larger $\phi \gg 1$, mixing occurs between ω_0 and ω_- . Thus, for large ω_r the mode coupling is small and mixing is spectrally forbidden. We characterize the regions of the complex ω plane with allowed hybridization by the red and green shaded regions in inset of Fig. 3(a), while spectrally inaccessible hybridization is denoted by κ_f . Based on this physical insight, the initially blueshifted $\tilde{\omega}_+$ behaving as a bright mode crosses the metal-insulator-metal eigenfrequency $\tilde{\omega}_{\text{MIM}}$ [indicated by the black dashed line in Fig. 3(a)], mixes with $\tilde{\omega}_0$ within the allowed region, and eventually evolves into nanocavity modes for larger ϕ . Conversely, the redshifted $\tilde{\omega}_-$, originating as a bifurcated mode, crosses the dark $\tilde{\omega}_{\text{MIM}}$ line and mixes with the original picocavity mode. We thus exploit this mixed mode evolution to elucidate spectral properties of the Green's function [2].

We reconstruct the spectral component of the Green's function as $\mathbf{G}(0, 0, \omega) \propto \sum_l [1/(\omega - \tilde{\omega}_l)]$ and evaluate the electromagnetic density of states and Purcell factor [36]. We confirm that our evaluated Green's function obeys Kramers-Kronig relations, as is clear from Figs. 3(b) and 3(c), and observe a regularized spectral evolution based on mixed hybrid-mode evolution. For $\phi \ll 1$, $\text{Im}[\mathbf{G}(0, 0, \omega)]$ gives two maxima corresponding to mixed $\tilde{\omega}_0$ and $\tilde{\omega}_-$ modes. For $\phi = 1.5$, we expect three frequency combs from the different excitation responses in Fig. 2, but find instead a double peak: a small peak from $\tilde{\omega}_-$ and a dominant peak from $\tilde{\omega}_0$. The latter is much larger than that from $\tilde{\omega}_+$, so the two peaks combine into a single Lorentzian peak. Interestingly, the peak from $\tilde{\omega}_-$ bifurcates and evolves into a Fano resonance [37]. For $\phi = 2.5$, the peak from $\tilde{\omega}_-$ asymptotically approaches $\tilde{\omega}_p = 1.56 + 0.007i$ eV and forms a stable picocavity mode with enhanced Purcell factor. In contrast, the other peaks contain a negligible electromagnetic density of states, as seen in Fig. 3.

V. PICOCAVITY FIELD QUANTIZATION AND ITS INTERACTION WITH A QUANTUM EMITTER

Following Green's function reconstruction, we now quantize fields inside the picocavity geometric volume Ω_p bounded by S_p , for which the picocavity-inside-NPOM structure acts as a leaky cavity. We must include radiative $P_{JJ'}^R$ and nonradiative $P_{JJ'}^{\text{NR}}$ decay in field quantization; hence, the quantized field does not follow the traditional quantum optics recipe. Here we assume the bosonic creation (annihilation) operator as $\hat{\mathbf{f}}(\mathbf{r}, \omega)$ [$\hat{\mathbf{f}}^\dagger(\mathbf{r}, \omega)$] and introduce the quantized electric field as $\hat{\mathbf{E}}(\mathbf{r}, \omega) = i\sqrt{\hbar/\pi\epsilon_0}(\omega/c)^2 \int d^3r' \mathbf{G}(\mathbf{r}, \mathbf{r}'; \omega) \cdot \hat{\mathbf{f}}(\mathbf{r}, \omega)$ [38]. To include nonradiative decay, we assume a volume

Ω within which picocavity modes are excited, using $\mathbf{G}(\mathbf{r}, \mathbf{r}'; \omega) = \sum_j \mathcal{A}_j(\omega) \tilde{\mathbf{E}}_j(\mathbf{r}) \tilde{\mathbf{E}}_j(\mathbf{r}')$ to obtain $[\hat{\mathbf{E}}(\mathbf{r}), \hat{\mathbf{E}}(\mathbf{r}')] = [\hat{\mathbf{E}}^\dagger(\mathbf{r}), \hat{\mathbf{E}}^\dagger(\mathbf{r}')] = 0$ and

$$[\hat{\mathbf{E}}(\mathbf{r}), \hat{\mathbf{E}}^\dagger(\mathbf{r}')] = \frac{\hbar}{\pi\epsilon_0} \sum_{JJ'} \tilde{\mathbf{E}}_J(\mathbf{r}) \cdot \tilde{\mathbf{E}}_{J'}^*(\mathbf{r}') \times \int_0^\infty d\omega \mathcal{B}(\omega) [P_{JJ'}^{\text{NR}}(\omega) + P_{JJ'}^{\text{R}}] \quad (6)$$

for $P_{JJ'}^{\text{NR}}(\omega) = \int d^3s \epsilon_{m,i}(s, \omega) \tilde{\mathbf{E}}_J(s) \tilde{\mathbf{E}}_{J'}^*(s)$ and $\mathcal{B}(\omega) = (\omega/c)^4 \mathcal{A}_J(\omega) \mathcal{A}_{J'}^*(\omega)$.

For $P_{JJ'}^{\text{R}}$, we assume $\hat{\mathbf{E}}_i(\mathbf{r}, \omega)$ and calculate (6) in component form $[\hat{E}_i(\mathbf{r}), \hat{E}_j^\dagger(\mathbf{r}')] \sim \sum_{qq'} \int_0^\infty d\omega (\omega/c)^4 \int d^3s \epsilon_m(s, \omega) G_{qi}(s, \mathbf{r}, \omega) G_{q'j}^*(s, \mathbf{r}', \omega)$. Specifically, we consider the Green's function definition in the component form $[\partial_q^s \partial_q^s - \delta_{qq'} (\Delta^s + (\omega/c)^2 \epsilon_m(s, \omega))] G_{qi}(s, \mathbf{r}, \omega) = \delta_{qi} \delta(s - \mathbf{r})$ [38,39], where $\partial^s := (\partial/\partial s)$ and Δ^s is the Laplacian, multiply this by $G_{q'j}^*(s, \mathbf{r}', \omega)$, and perform volume integration. Then we use integration by parts and the divergence theorem [40] and assume that the Green's functions of hybrid modes are zero at the \mathbf{r}_0 . We employ $i \leftrightarrow j$ and $\mathbf{r} \leftrightarrow \mathbf{r}'$ and perform complex conjugation of the resultant equation to obtain the radiative part as $P_{JJ'}^{\text{R}} = \int dA [\partial^s \tilde{\mathbf{E}}_J(s) \cdot \tilde{\mathbf{E}}_{J'}^*(s) - \partial^s \tilde{\mathbf{E}}_{J'}^*(s) \cdot \tilde{\mathbf{E}}_J(s)]$. Interestingly, Eq. (6) includes field hybridization to quantization. Assuming $\hat{\mathbf{E}}(\mathbf{r}) = \sum_j \tilde{\mathbf{E}}_j(\mathbf{r}) \hat{\zeta}_j + \text{H.a.}$, we achieve, from (6), $[\hat{\zeta}_j, \hat{\zeta}_{j'}^\dagger] = (\mathbf{P})_{JJ'}$. Correspondence between this commutation relation and the bosonic commutation relation $[a_j, a_{j'}^\dagger] = \delta_{jj'}$ allows us to define creation and annihilation operators as

$$a_j = \sum_{j'} (\mathbf{P})_{JJ'}^{-1/2} \hat{\zeta}_{j'}, \quad a_j^\dagger = \sum_{j'} (\mathbf{P})_{JJ'}^{-1/2} \hat{\zeta}_{j'}^\dagger. \quad (7)$$

For $\tilde{\omega}_- \approx \tilde{\omega}_p$ forming a stable cavity mode, we obtain, through the use of (7), $\hat{\zeta}_p = (\mathbf{P}^{1/2})_{pp} a$ for $a := a_p$ and $\hat{\mathbf{E}} = (\mathbf{P}^{1/2})_{pp} \tilde{\mathbf{E}}_p(\mathbf{r}) a + \text{H.a.}$, which provides a framework towards the picoscopic light-matter interaction.

We note that the stability of the quantized picocavity mode depends on dissipation. Thus the possibility of dissipative mode quantization (for various ϕ) can be qualitatively interpreted in terms of different orders of perturbation. Lower radiative and nonradiative losses for $\phi = 2.5$ [see Fig. 3(a)] correspond to zeroth-order perturbation, for which our formalism for picocavity mode quantization is valid. Indeed, for low radiative and nonradiative losses, as for $2 < \phi < 2.5$, losses related to the picocavity field quenching to the nanoparticle and nanocavity QNM excitation become negligible, which corresponds to first-order perturbation. We note that our quantization formalism incorporates radiative and nonradiative loss channels, i.e., $P_{JJ'}^{(i)}$, $i \in \{\text{R}, \text{NR}\}$, and in this case is still applicable for picocavity mode quantization. However, the case $1 < \phi < 2$ is related to large dissipation, which corresponds to higher-order perturbation; in this case, the picocavity QNM can lead to nanocavity QNM excitation (due to the resonant condition $\tilde{\omega}_p \approx \omega_m$) affecting quantization. Thus, including a large dissipation into our quantization formalism and its perturbation interpretation requires further consideration that can be addressed in future work.

Based on the field evolution and quantization framework, a two-level quantum emitter can interact with quantized fields, specifically with the $\tilde{\omega}_p = 1.56 + 0.007i$ eV mode, representing the light-matter interaction at the picoscale. For the two-level quantum emitter approximation, standard methods of light-matter interaction, such as those outlined in Refs. [9,10], should be applied. However, the effects of leakage and mode hybridization must be incorporated into the quantization of the picocavity field, as these factors influence the interaction between the quantized picocavity mode and the two-level quantum emitter. To model this interaction, we consider the emitter as part of a molecule, treated here as a pointlike dipole, e.g., conjugated bonds at the molecule's tail or an emissive lanthanide defect atom within the molecule, interacting with the picocavity's dipolar field. Molecular size effects [21,22] are neglected in this context, meaning the picocavity fields interact only with the pointlike dipole and not with the entirety of the molecule's orbitals. As such, the dipole approximation is sufficient for this analysis. Discussions concerning stable interactions between the entire molecule and picocavity fields, which could induce chemical modifications via changes in molecular vibrational spectra [41], are beyond the scope of this study and are not considered here.

To test the feasibility of the interaction between a quantum emitter and quantized picocavity mode, we consider a single-mode quantized picocavity field with excitation frequency ω_- and a assume two-level quantum emitter with ground (excited) state $|g\rangle$ ($|e\rangle$), of excitation frequency ω_{eg} and decay rate Γ_{eg} . Then the total Hamiltonian of the system is $H_{\text{sys}} = H_a + H_{\text{pl}} + H_{\text{int}}$, where $H_a = \omega_{eg}\sigma^+\sigma^-$ is the quantum emitter Hamiltonian, with σ^+ (σ^-) the raising (lowering) operator, $H_{\text{pl}} = \omega_- a^\dagger a$ is the quantized picocavity field Hamiltonian, and $H_{\text{int}}(\omega) = g(\mathbf{r}, \omega)(\sigma^+ a + \sigma^- a^\dagger)$ is the interaction Hamiltonian, with $g(\mathbf{r}, \omega)$ the coupling constant between the two-level system and picocavity mode.

In this work we are interested in the temporal evolution of the quantum emitters; hence, the evolution corresponding to the picocavity field must be traced out. To this aim, we use the general framework of open quantum systems [42], treating the picocavity as the bath (with bath operator \mathbf{B}) and quantum emitter as a system (with system operator \mathbf{S}). Specifically, we define $\mathbf{S} = \sigma^+ + \sigma^-$ and $\mathbf{B} = g(\mathbf{r}, \omega)(a + a^\dagger)$ to express the interaction Hamiltonian as $H_{\text{int}} = \mathbf{S} \otimes \mathbf{B}$. In the interaction picture with respect to $H_a + H_{\text{pl}}$, we apply the mappings $a \mapsto ae^{-i\omega t}$ and $\sigma^\pm \mapsto \sigma^\pm e^{\pm i\omega_{eg} t}$. According to the standard formalism of the light-matter interaction, all information related to the interaction between a dissipative quantized mode and a quantum emitter is reflected in the spectral density defined as $g(\mathbf{r}_0, \omega) = \sqrt{J(\omega)}$ [43]. The electromagnetic density of states $J(\omega)$ in turn is part of the interaction Hamiltonian

$$H_{\text{int}} = \sqrt{J(\omega)}(\sigma^+ a + \sigma^- a^\dagger). \quad (8)$$

In our picocavity-inside-NPOM case discussed here, $g(\mathbf{r}, \omega)$ depends on the spatial distribution of the picocavity field [see Fig. 4(a)] and the optical density of states, providing the interaction for nonvanishing picocavity field $\mathbf{E}_p(\phi) \neq 0$ and picocavity density of states $J(\omega) \propto \text{Im}[G(\omega)]$. We thus

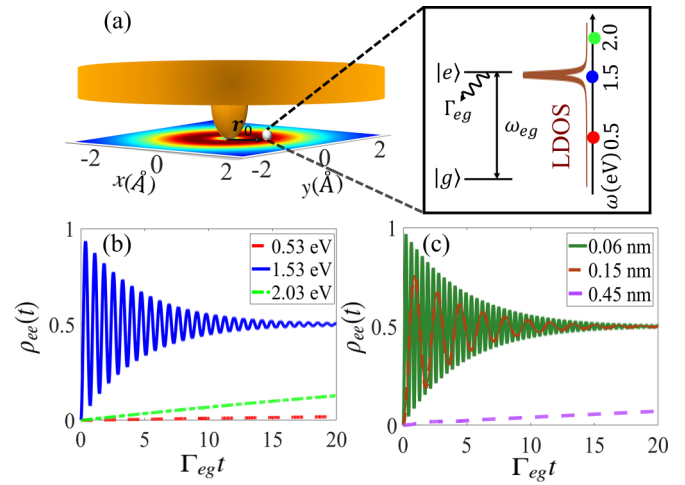


FIG. 4. Picoscopic light-matter interaction. (a) Field distribution at $\tilde{\omega}_p = 1.56 + 0.007i$ eV. An atomistic two-level quantum emitter (integrated into a larger molecule) is situated at a distance r_0 from the picocavity. The inset shows energy levels of the quantum emitter. The brown curve is the density of states for $\tilde{\omega}_-$ and $\phi = 2.5$. Also shown is the excited-state ρ_{ee} occupation for (b) various transition frequencies ω_{eg} and (c) different r_0 . Here time is scaled to $\tau_0 = 10$ fs.

proceed with the resulting interaction Hamiltonian H_{int} and calculate the evolution of the atomic-state occupation $\rho_{ee}(t)$ using the master equation $\partial_t \rho = i[H_{\text{int}}, \rho] + \sum_j \mathcal{L}_j[\rho]$. Here $\mathcal{L}_j[\rho]$ gives the incoherent Lindblad terms corresponding to the operator \mathbf{O} considered as $\mathcal{L}_j[\rho] = (\gamma_j/2)(2\mathbf{O}\rho\mathbf{O}^\dagger - \{\mathbf{O}^\dagger\mathbf{O}, \rho\})$ [41]. We assume a simple case, where the picocavity has a dissipation \mathcal{L}_a due to nonradiative decay $\gamma_{\text{NR}} \approx 2 \text{Im}[\varepsilon_m(\omega)]|\tilde{\alpha}_z(\omega_{\text{res}})|^2/[\hbar|\varepsilon_m(\omega) - \varepsilon_g|^2]$ [44] and the two-level system has a dissipation \mathcal{L}_σ due to frequency-dependent decay $\Gamma_{eg}(\omega)$. We then evaluate the occupation of the excited state $\rho_{ee}(t)$ for $\phi = 2.5$, corresponding to an enhanced local density of states, and assume $\omega_{eg} \approx 1.5$ eV. Therefore, our atom resonantly interacts only with the $\tilde{\omega}_p$ mode. We further assume that the atom is in the ground state at $t_0 = 0$, i.e., $\rho_{gg}(t_0) = 1$, and $\rho_{ee}(t_0) = 0$, with no atomic excitation in the system, allowing us to obtain oscillatory Jaynes-Cummings-like dynamics by fine-tuning the transition frequency of the two-level system and its distance from the center of picocavity ($r_0 = |\mathbf{r} - \mathbf{r}'|$), as clearly shown in Figs. 4(b) and 4(c).

The outlined calculation serves primarily as a validation of the Jaynes-Cummings model for picoscopic light-matter interactions. To examine the contribution of the picocavity mode to quantum dynamics, we focus on a resonant interaction between the quantized picocavity field $\phi = 2.5$ and a quantum emitter, where nanocavity QNMs are off-resonant and thus do not influence the quantum dynamics. However, our formalism can also be applied to investigate interactions between a quantum emitter and a hybridized field in the limiting case of $\phi \ll 1$. This scenario, contrasting with our current focus, would explore the dynamics of a quantum emitter within the NPOM system when the picocavity mode does not contribute to the interaction. We leave this case for future work (see

Ref. [45]) or a realistic example of dipole interactions with NPOM modes.³

To establish the Jaynes-Cummings framework for picoscopic light-matter interactions, we neglect effects related to electron kinetics and the physical size of the quantum emitter. Consequently, we do not directly predict emission or absorption within this dipole approximation, as higher-order poles and molecular-size effects might become significant [21,22]. For instance, at separations as small as 0.6 Å as in Fig. 4(a), lanthanide emitters are integrated into NPOMs [46], though additional quantum effects, such as charge transfer, may arise for many emitters. Furthermore, according to the kinetic theory of electron gases, the accumulated energy within the metal electrons can lead to nonexponential decay in the quantum emitter, impacting its quantum dynamics.

VI. CONCLUSION AND OUTLOOK

In this work, we presented a multiscattering-based formalism that offers insights into the modal evolution and quantization of the picocavity-inside-NPOM configuration. By introducing a generalized coupled-mode theory and quantizing the leaky picocavity modes, our approach addresses three fundamental challenges in nano- and picophotonics: (i) calculating the electromagnetic fields within nanostructures, (ii) modeling a single gold atom on the facet of a nanoparticle, and (iii) understanding the dynamic evolution of a quantum emitter near a picocavity. Unlike previous studies [4,6–9], our framework integrates these issues through a unified coupled-mode formalism that analyzes the interaction of multiple nanocavity QNMs with a single picocavity QNM. This is grounded in the premise that localized plasmon polarizations can be effectively described using electromagnetic wave theory, with the electric field governed by the kinetics of electrons in the picocavity-inside-NPOM system.

A key strength of our approach is its ability to reveal the interconnection of nanocavity modes through mode hybridization, leading to spectral correlations among hybrid modes. This field-field interaction merges discrete nanocavity spectra with the continuous spectrum of the picocavity, resulting in the enhanced normal-mode splitting of up to 350 meV, indicative of strong mode coupling. Hybrid modes in the complex spectral domain evolve based on the overlap between pico- or nanocavity QNMs and frequency detunings, creating both allowed and forbidden couplings. By reconstructing the self-interaction Green's function, we demonstrate that intermediate hybrid modes spectrally mix high- and low-energy branches as the aspect ratio is tuned. Hybridization with the high-energy branch produces a single Lorentzian peak for the Purcell factor, while the low-energy branch bifurcates into a Fano resonance, ultimately stabilizing as a distinct picocavity mode.

³A potential approach to investigate the controllable interaction between a quantum emitter and both pico- and nanocavity QNMs is to consider a three-level quantum emitter, with each transition resonantly coupling to either the picocavity or NPOM modes. The specific case of $\phi \ll 1$ can represent a scenario where the coupling between the picocavity and the quantum emitter is suppressed.

To further illustrate the applicability of our formalism, we employ the Lindblad master equation to model a two-level quantum emitter positioned spatially and spectrally near a stable $\tilde{\omega}_-$ picocavity mode. Notably, our coupled-mode framework successfully retrieves Jaynes-Cummings-like dynamics by fine-tuning the frequency and position of the two-level system, showcasing its robustness in capturing quantum dynamics within picocavity systems.

In configurations with intricate geometries, such as picocavity-inside-NPOM setups, electron dynamics kinetics introduces nonlocality [47,48] impacting both the picocavity mode and its interaction with a quantum emitter. Nonlocality manifests as Landau damping, influencing field enhancement [47,49], and, within certain energy ranges, may also lead to nonexponential decay of a quantum emitter due to energy accumulation in the electron gas. These factors play a significant role and must be accounted for, especially in cases where quantum emitters are positioned at subnanometer distances from protrusions. Therefore, incorporating the electron gas kinetics through the Boltzmann kinetic equation as an explicit framework [47], using approximations such as quantum hydrodynamics [14], or applying quantum surface corrections to QNM algebra [15] in our generalized quasinormal coupled-mode theory should provide better accuracy, a refinement that may be considered in future research. Moreover, the quantum dynamics between the quantum emitter and the quantized picocavity mode warrant thorough investigation. Nonexponential behavior due to the linear response of the electron gas [47] and the role of plasmon memory associated with the picocavity density of states are two distinct mechanisms that could lead to a complex non-Markovian evolution of the quantum emitter-picocavity field system [42,50]. Regarding plasmon memory, the picocavity density of states could result in reabsorption and reemission of the plasmon field by the quantum emitter [51–53] which might influence energy accumulation within the electron gas. Including memory kernels for light-matter interactions and considering the molecular-size effect on quantum dynamics between the two-level emitter and picocavity field could be valuable directions for future work. In summary, representing the picocavity mode as a QNM, along with the QNMs of a nanocavity, within an electromagnetic framework for the picocavity-inside-NPOM configuration provides valuable qualitative insights into near-field characteristics. This approach enables the exploration of picocavity mode hybridization, spectral correlations, and leaky mode quantization, thereby opening new avenues for investigating the dynamic interaction between quantized picocavity QNM(s) and two-level quantum emitters.

ACKNOWLEDGMENTS

O.H. gratefully acknowledges funding from Research Ireland (formerly Science Foundation Ireland) via the METAQUANT Research Professorship Programme (Grant No. 18/RP/6236). S.A.-Z. acknowledges eINIS and TCHPC for providing computational resources. J.J.B. acknowledges funding from Horizon 2020 research and innovation programs PICOFORCE (Grant Agreement No. 883703) and POSEIDON (Grant Agreement No. 861950) and UK EPSRC EP/X037770/1.

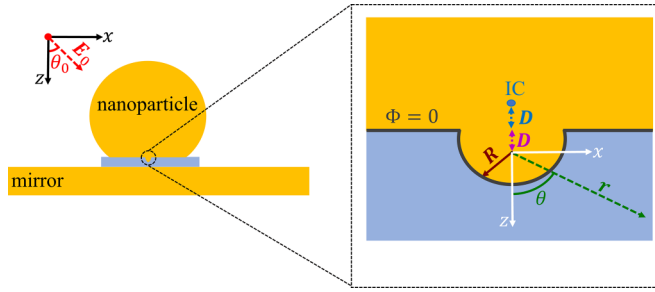


FIG. 5. Picocavity-inside-NPOM configuration, illuminated with an external field E_0 at an angle θ_0 . For our Laplace equation formalism, we assume a picocavity with radius R formed on the facet of the nanoparticle. The origin of the coordinate is then matched with the center of the picocavity, and the position of the facet would then be fixed at $z = -D$. To satisfy the general boundary condition, we also assume an image charge (IC, indicated in the inset) at $z = -2D$, which provides zero potential $\Phi = 0$ (represented by the gray line $\Phi = 0$ in the inset) at the interaction surfaces.

APPENDIX A: POLARIZABILITY OF A TRUNCATED SPHERE IN THE FACET OF THE NANOPARTICLE

In this Appendix we utilize an approach similar to that presented in Ref. [6] to calculate the polarizability of a picocavity using the solution to the Laplace equation. To maintain self-consistency in our work, we present the detailed quantitative steps in our analysis. Here we approximate the picocavity as a truncated sphere situated on the facet of the nanoparticle, as shown in Fig. 5. We choose the center of the picocavity as the origin of the Cartesian coordinate system. The picocavity has radius R and the nanoparticle facet is located at $z = -D$, with $D > R$. The width of the facet is also much bigger than the size of the picocavity. Following Ref. [6], we also assume an image charge at $z = -2D$ to provide a boundary condition $\Phi(r, \theta) = 0$, with θ the polar angle in spherical coordinates, at the surfaces of both the facet and the picocavity (gray line in Fig. 5). Finally, the picocavity-inside-NPOM structure is illuminated by a weak electric field $\mathbf{E}_0 = E_0(\sin \theta_0, 0, \cos \theta_0)$. For arbitrary point $\mathbf{r} = |\mathbf{r}|(\sin \theta \cos \varphi, 0, \cos \theta)$, the scalar potential due to this weak field is given by $\Phi_\infty(r, \theta, \varphi) = E_0 r(\cos \theta \cos \theta_0 + \sin \theta \sin \theta_0 \cos \varphi)$.

Following previous works [31], we assume that the NPOM modes can be expressed in terms of spherical harmonics $Y_l^m(\theta, \varphi)$ for $l \in \{1, 2, 3, \dots\}$ and $-l \leq m \leq l$. Assuming $E_0 = 1$ V/m, we express the general solution of the potential for points outside the protuberance and in the dielectric layer as

$$\Phi_d(r, \theta, \varphi) = \sum_{l=0}^{\infty} \sum_{m=-l}^l (r^l \mathcal{D}_{lm} + r^{-l+1} \mathcal{C}_{lm}) Y_l^m(\theta, \varphi). \quad (\text{A1})$$

Using the boundary condition at $r \rightarrow \infty$ where $\Phi_d(r, \theta, \varphi) = \Phi_\infty(r, \theta, \varphi)$ and expressing spherical harmonics in terms of Legendre polynomials

$$Y_l^m(\theta, \varphi) = \sqrt{\frac{(2l+1)(l-m)!}{4\pi(l+m)!}} P_l^m(\cos \theta) e^{im\varphi},$$

we obtain $m \in \{0, 1\}$ as possible solutions. Consequently, Eq. (A1) reduces to

$$\begin{aligned} \Phi_d(r, \theta, \varphi) &= r \cos \theta \cos \theta_0 + r \sin \theta \sin \theta_0 \cos \varphi \\ &+ \sum_{l=1}^{\infty} r^{-(j+1)} (\mathcal{C}_{1j} P_j^0 + \mathcal{C}'_{1j} P_j^1 \cos \varphi) + \Phi_{\text{IC}}^d, \end{aligned} \quad (\text{A2})$$

where $P_l^m(\eta) = (1 - \eta^2)^{(m/2)} / (2^l l!) (d/d\eta)^{l+m} (\eta^2 - 1)^l$ are defined as the associated Legendre functions and we have used $\Phi_{\text{IC}}^d := \Phi_{\text{IC}}^d(r, \theta, \varphi)$ and $P_j^m := P_j^m(\cos \theta)$ as abbreviations. Here $\Phi_{\text{IC}}^d(r, \theta, \varphi)$ is the potential due to the image charge that satisfies the boundary condition.

We note that the scalar potential due to the image charge must be chosen to ensure that the total potential at the boundary, as characterized in Fig. 5, is zero, which is achieved by assuming the potential due to this image charge as

$$\Phi_{\text{IC}}^d = \sum_{j=1}^{\infty} [\mathcal{I}_{1j} \mathcal{V}_j^0(r, \cos \theta) + \mathcal{I}'_{1j} \mathcal{V}_j^1(r, \cos \theta) \cos \varphi]. \quad (\text{A3})$$

We characterize $\mathcal{V}_j^m(r, \cos \theta)$ explicitly by setting $\mathbf{r}' = (0, 0, -2D)$ as the coordinate of the image charge. We then obtain $\cos \theta = z_{r'}/|\mathbf{r} - \mathbf{r}'|$, where

$$|\mathbf{r} - \mathbf{r}'| = (r^2 - 4rD \cos \theta_{r'} + 4D^2)^{1/2},$$

with $\theta_{r'} = \pi - \theta$, and $z_{r'} = 2D - r \cos \theta$. Finally, by equating $r^{-(j+1)} P_j^m(\cos \theta) = \mathcal{V}_j^m(r, \cos \theta)$ for $r = |\mathbf{r} - \mathbf{r}'|$, we obtain

$$\begin{aligned} \mathcal{V}_j^m(r, \cos \theta) &= (r^2 - 4rD \cos \theta + 4D^2)^{-(j+1)/2} \\ &\times P_j^m \left(\frac{2D - r \cos \theta}{\sqrt{r^2 - 4rD \cos \theta_{r'} + 4D^2}} \right). \end{aligned} \quad (\text{A4})$$

Similar to (A2), we introduce the scalar potential for $r > R$ in the metallic nanoparticle as

$$\begin{aligned} \Phi_m(r, \theta, \varphi) &= \Phi_{\text{mc}} + \alpha r \cos \theta \cos \theta_0 + \beta r \sin \theta \sin \theta_0 \cos \varphi \\ &+ \sum_{l=1}^{\infty} r^{-(j+1)} (\mathcal{M}_{1j} P_j^0 + \mathcal{M}'_{1j} P_j^1 \cos \varphi), \end{aligned} \quad (\text{A5})$$

where Φ_{mc} , α , and β are constants that we can explicitly characterize using boundary conditions between the dielectric and the facet of the nanoparticle. Note that the image charge does not play a role in the potential inside the nanoparticle; therefore, we set $\Phi_{\text{IC}}^m = 0$. Then assuming that the scalar potential inside the picocavity should be finite, namely, removing coefficients related to $r^{-(j+1)}$ in Eq. (A1), we obtain the general solution of the Laplace equation inside the protrusion as

$$\begin{aligned} \Phi_p(r, \theta, \varphi) &= \Phi_{\text{pc}} + \Phi_{\text{IC}}^p \\ &+ \sum_{l=1}^{\infty} r^j (\mathcal{P}_{1j} P_j^0 + \mathcal{P}'_{1j} P_j^1 \cos \varphi). \end{aligned} \quad (\text{A6})$$

Finally, following a similar line of reasoning that yields Eq. (A3), we express $\Phi_{\text{IC}}^{\text{p}}$ as

$$\Phi_{\text{IC}}^{\text{p}} = \sum_{j=1}^{\infty} [\mathcal{J}_{1j} \mathcal{W}_j^0(r, \cos \theta) + \mathcal{J}'_{1j} \mathcal{W}_j^1(r, \cos \theta) \cos \varphi]. \quad (\text{A7})$$

Our derived scalar potential described by Eqs. (A2), (A5), and (A6) is analogous to that obtained in Ref. [6], as both describe a truncated emitter on a flat substrate. Consequently, spherical harmonics and associated Legendre polynomials can be considered as a complete set for representing the scalar potential. Thus, we can leverage general boundary conditions to characterize the scalar potential of the picocavity. Specifically, according to classical electromagnetic theory, the facet of the nanoparticle and surface of the picocavity must satisfy two general boundary conditions: continuity of the potential at $z = -D$ and $r = R$. To apply these boundary conditions for our design, we need to characterize \mathcal{V}_j^m and \mathcal{W}_j^m in Eqs. (A2) and (A6), respectively. Given that $\mathbf{r}' = (0, 0, -2D)$, we derive the relations $z = r \cos \theta - 2D$, $\cos \theta = D/r$, and $r \sin \theta = [r^2 - D^2]^{1/2}$. Substituting these expressions into (A4), we obtain

$$\mathcal{V}_j^0\left(r, \frac{D}{r}\right) = (-1)^{-j} \frac{P_j^0(D/r)}{r^{-(j+1)}},$$

$$\mathcal{V}_j^1\left(r, \frac{D}{r}\right) = (-1)^{-(j+1)} \frac{P_j^1(D/r)}{r^{-(j+1)}}.$$

Next we substitute these results into Eqs. (A2) and (A5), setting $\Phi_{\text{d}}(r, \theta, \varphi) = \Phi_{\text{m}}(r, \theta, \varphi)$. In addition to the continuity of the scalar potential, we must also consider the continuity of the normal component of the displacement vector, which for the picocavity-inside-NPOM structure can be expressed as

$$\varepsilon_{\text{g}} \partial_z \Phi_{\text{d}}(r, \theta, \phi)|_{D=r \cos \theta} = \varepsilon_{\text{m}}(\omega) \partial_z \Phi_{\text{m}}(r, \theta, \phi)|_{D=r \cos \theta}.$$

We then plug the scalar potential from (A2), and (A5) into these boundary conditions, achieving $\alpha = \varepsilon_{\text{g}}/\varepsilon_{\text{m}}(\omega)$, $\beta = 1$, $\Phi_{\text{IC}}^{\text{d}} = (1 - \alpha)D \cos \theta$, and

$$\mathcal{I}_{1j} = (-1)^j \frac{\varepsilon_{\text{g}} - \varepsilon_{\text{m}}(\omega)}{\varepsilon_{\text{g}} + \varepsilon_{\text{m}}(\omega)} \mathcal{C}_{1j}. \quad (\text{A8})$$

We note that this boundary condition does not include the orthogonality of the spherical harmonics related to QNM theory and hence our expressions in the derivation of the boundary condition at $z = -D$ are similar to those in Ref. [6].

Despite the similarity in approach and successful application for $z = -D$, we must now note that the boundary condition recipe presented in Ref. [6] at $r = R$ is not generally applicable within the framework of QNM algebra. Indeed, while our mathematical formulation of spherical harmonics and associated Legendre functions is similar, the normalization, orthogonality, and completeness of these modes that adhere to QNM algebra differ significantly from the normal modes assumed in Ref. [6]. Therefore, although the boundary conditions introduced in that reference might be applicable to our quantitative analysis, spherical harmonics specific to the NPOM structure must also satisfy the boundary condition related to QNM algebra. Specifically, QNMs are subject to perfectly matched layers, influencing their orthogonality, normalization, and completeness. Including explicit contributions due to QNM algebra on the scalar potential falls outside the scope of our present work.

Quantitatively, we note that spherical harmonics in Ref. [6] are assumed to form a complete orthogonal set, with the orthogonality condition given by

$$\int_{-1}^1 dt P_l^m(t) P_k^m(t) = \frac{2(j+m)!}{(2j+1)(j-m)!} \delta_{jk}, \quad (\text{A9})$$

where $t = \cos \theta$. This condition differs significantly from the orthogonality condition of the QNM algebra that we used in our work

$$\int_{V_{\text{eff}}} dV Y_l^{n*} [\tilde{\omega}_m \varepsilon_{\text{m}}(\tilde{\omega}_m) - \tilde{\omega}_n \varepsilon_{\text{m}}(\tilde{\omega}_n)] Y_l^m \simeq \delta_{mn}. \quad (\text{A10})$$

Consequently, the approach taken in Ref. [6], which involves multiplying P_k^0 (or Y_k^0) by $(\Phi_{\text{d}} - \Phi_{\text{p}})_{r=R}$ and integrating over all azimuthal and polar angles appears to be inaccurate for nanometer and subnanometer structures.

A better accuracy can be obtained by utilizing (A10) instead of (A9); however, this analysis requires careful integration over azimuthal and polar angles, as well as spatial integration over perfectly matched layer regions. Consequently, boundary conditions related to $r = R$ cannot be exploited to also fix the scattering boundary conditions.

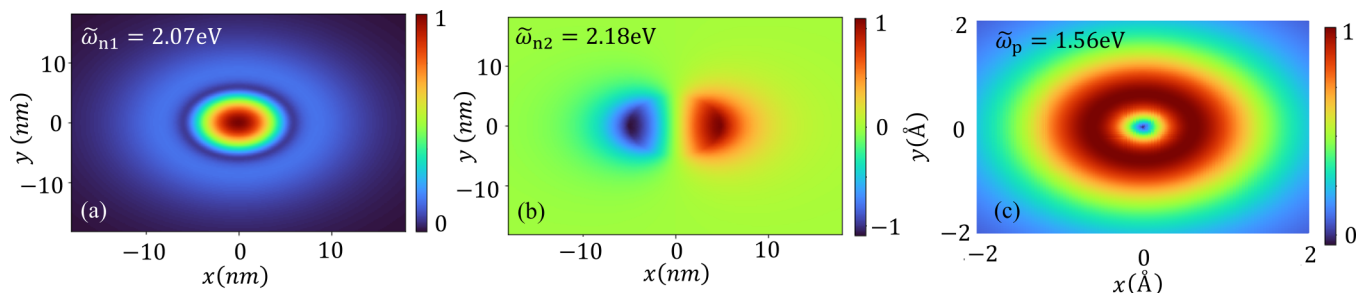


FIG. 6. The z -component electric field of the normalized nanocavity and picocavity QNMs. (a) Spatial distribution of $\tilde{E}_{n1}(x, y)$ corresponding to $\tilde{\omega}_{n1}$ and (b) field profile of $\tilde{E}_{n2}(x, y)$ corresponding to $\tilde{\omega}_{n2}$ eigenfrequencies. (c) The z component of the picocavity QNM $\tilde{E}_{\text{p}}(x, y)$. The color bar in each panel represents the normalized field intensity $E_{zj}/|E_{m,\text{max}}|$, with $m \in \{n1, n2, \text{p}\}$, and for $|E_{m,\text{max}}|$ the maximum of the field corresponds to nanocavity-picocavity QNMs. In these simulations, we assume $2R = 80$ nm as the nanoparticle radius, $w = 10$ nm as the facet width, $d = 1$ nm as the gap size, $n_{\text{g}} = 1.45$ as the gap index, $\phi = 2.5$, and $z = 0.35$ nm.

Despite quite dissimilar orthogonality conditions, Eq. (A9) can still yield a mathematical expression for the polarizability of the picocavity-inside-NPOM configuration, which is analogous to the one derived via spectral representation. Hence, in the following, we use the traditional orthogonality relation (A9) to calculate the polarizability of the truncated sphere (assumed here as a picocavity).

For our specific architecture, by disregarding the QNM orthogonality and by assuming $t = \cos \theta$, we express the boundary condition at $r = R$ as

$$\int_{-1}^R dt \int_0^{2\pi} d\varphi (\Phi_d - \Phi_p)_{r=R} P_k^0(t) = 0. \quad (\text{A11})$$

Next we substitute Φ_d and Φ_p using (A2) and (A6), respectively, in this equation and utilize the relation

$$\mathcal{J}_{1j} = (-1)^j \frac{\varepsilon_g - \varepsilon_m(\omega)}{\varepsilon_g + \varepsilon_m(\omega)} \mathcal{P}_{1j}$$

and orthogonality of the Legendre polynomials for different m , namely, $\int_0^{2\pi} P_j^1(t) P_k^0(t) \cos \varphi d\varphi = 0$, and also (A9) to obtain the characteristic equation

$$\sum_{j=1}^{\infty} C_{kj} \mathcal{C}_{1j} - 2\Phi_{mc} \delta_{k0} = E_k \cos \theta_0 \quad (\text{A12})$$

for

$$C_{kj} = \frac{4\varepsilon_g}{(2k+1)[\varepsilon_g + \varepsilon_m(\omega)]} \delta_{jk} - \frac{\varepsilon_g - \varepsilon_m(\omega)}{\varepsilon_g + \varepsilon_m(\omega)} \int_{-1}^R dt [P_j^0(t) - (-1)^j V_j^0(1, t)] P_k^0(t). \quad (\text{A13})$$

An expression similar to (A12) can then be readily derived for \mathcal{P}_{1j} coefficients. We define the polarizability along the z axis as

$$\alpha_z = -\frac{\varepsilon_g R^3}{\varepsilon_0 \cos \theta_0} \mathcal{C}_{11}. \quad (\text{A14})$$

Assuming a truncated sphere on the facet, we can utilize the identity [6]

$$V_j^m(r, t) = (-1)^{j+m} \sum_{l=m}^{\infty} \frac{(l+j)! r^l P_l^m(t)}{(l+m)!(j-m)!(2D)^{l+j+1}}. \quad (\text{A15})$$

Then we define the average ($\bar{\varepsilon}$) and relative ($\delta\varepsilon$) permittivity as $\bar{\varepsilon} := \varepsilon_g + \varepsilon_m(\omega)$ and $\delta\varepsilon := \varepsilon_g - \varepsilon_m(\omega)$ and truncate the spherical harmonic expansion to dipole approximation, which allows us to express \mathcal{C}_{11} as

$$\mathcal{C}_{11} = \frac{\delta\varepsilon/(\varepsilon_g + \bar{\varepsilon})}{1 - (1/4)[(\delta\varepsilon)^2/\bar{\varepsilon}(\varepsilon_g + \bar{\varepsilon})]}. \quad (\text{A16})$$

Finally plugging this equation into (A14), we obtain the polarizability along the z axis as

$$\alpha_z(\omega) = \varepsilon_0 V_{\text{sp}} \frac{\varepsilon_m(\omega) - \varepsilon_g}{\varepsilon_g + L_z[\varepsilon_m(\omega) - \varepsilon_g]}, \quad (\text{A17})$$

which, apart from the geometrical factor L_z , is the same as Eq. (1) achieved using the spectral representation [19].

APPENDIX B: FIELD PROFILE OF THE PICOCAVITY AND NANOCAVITY QNMS

As indicated in Sec. IV, the NPOM structure has two modes with considerable overlap with the picocavity QNM, namely, a bright mode with resonant frequency $\tilde{\omega}_{n1} \approx 2.07$ eV and a dark mode corresponding to $\tilde{\omega}_{n2} \approx 2.18$ eV. Based on the nomenclature description of the NPOM structure presented in Appendix A, we denote that the z -component electric-field profile of $\tilde{\omega}_{n1}$ is indeed spherically harmonic and spatially distributed with bright circular symmetry [Fig. 6(a)], while $\tilde{\omega}_{n2}$ is antisymmetric with odd spatial distribution [Fig. 6(b)], which is in agreement with previous modal analysis of an NPOM structure [31]. We note that the picocavity is an elongated ellipsoid whose radiation we approximate with a dipolar reradiation; therefore, the picocavity QNM should have a spatial distribution of a dipolar radiation pattern, as indicated in Fig. 6(c).

-
- [1] Q. Lin, S. Hu, T. Földes, J. Huang, D. Wright, J. Griffiths, E. Elliott, B. de Nijs, E. Rosta, and J. J. Baumberg, Optical suppression of energy barriers in single molecule-metal binding, *Sci. Adv.* **8**, eabp9285 (2022).
- [2] L. A. Jakob, W. M. Deacon, Y. Zhang, B. de Nijs, E. Pavlenko, S. Hu, C. Carnegie, T. Neuman, R. Esteban, J. Aizpurua, and J. J. Baumberg, Giant optomechanical spring effect in plasmonic nano- and picocavities probed by surface-enhanced Raman scattering, *Nat. Commun.* **14**, 3291 (2023).
- [3] F. Benz, M. K. Schmidt, A. Dreismann, R. Chikkaraddy, Y. Zhang, A. Demetriadou, C. Carnegie, H. Ohadi, B. de Nijs, R. Esteban, J. Aizpurua, and J. J. Baumberg, Single-molecule optomechanics in “picocavities”, *Science* **354**, 726 (2016).
- [4] J. J. Baumberg, Picocavities: A primer, *Nano Lett.* **22**, 5859 (2022).
- [5] J. Langer, D. J. de Aberasturi, J. Aizpurua, R. A. Alvarez-Puebla, B. Auguié, J. J. Baumberg, G. C. Bazan, S. E. J. Bell, A. Boisen, A. G. Brolo *et al.*, Present and future of surface-enhanced Raman scattering, *ACS Nano* **14**, 28 (2020).
- [6] M. M. Wind, J. Vlieger, and D. Bedeaux, The polarizability of a truncated sphere on a substrate I, *Physica A* **141**, 33 (1987).
- [7] C. Tserkezis, R. Esteban, D. O. Sigle, J. Mertens, L. O. Herrmann, J. J. Baumberg, and J. Aizpurua, Hybridization of plasmonic antenna and cavity modes: Extreme optics of nanoparticle-on-mirror nanogaps, *Phys. Rev. A* **92**, 053811 (2015).
- [8] J. J. Baumberg, J. Aizpurua, M. H. Mikkelsen, and D. R. Smith, Extreme nanophotonics from ultrathin metallic gaps, *Nat. Mater.* **18**, 668 (2019).
- [9] V. V. Klimov and M. Ducloy, Spontaneous emission rate of an excited atom placed near a nanofiber, *Phys. Rev. A* **69**, 013812 (2004).

- [10] D. E. Chang, A. S. Sørensen, P. R. Hemmer, and M. D. Lukin, Strong coupling of single emitters to surface plasmons, *Phys. Rev. B* **76**, 035420 (2007).
- [11] P. Lodahl, S. Mahmoodian, and S. Stobbe, Interfacing single photons and single quantum dots with photonic nanostructures, *Rev. Mod. Phys.* **87**, 347 (2015).
- [12] J. Griffiths, B. de Nijs, R. Chikkaraddy, and J. J. Baumberg, Locating single-atom optical picocavities using wavelength-multiplexed Raman scattering, *ACS Photonics* **8**, 2868 (2021).
- [13] M. Urbieto, M. Barbry, Y. Zhang, P. Koval, D. Sánchez-Portal, N. Zabala, and J. Aizpurua, Atomic-scale lightning rod effect in plasmonic picocavities: A classical view to a quantum effect, *ACS Nano* **12**, 585 (2018).
- [14] W. Li, Q. Zhou, P. Zhang, and X.-W. Chen, Bright optical eigenmode of 1 nm^3 mode volume, *Phys. Rev. Lett.* **126**, 257401 (2021).
- [15] T. Wu, W. Yan, and P. Lalanne, Bright plasmons with cubic nanometer mode volumes through mode hybridization, *ACS Photonics* **8**, 307 (2021).
- [16] C. Tao, J. Zhu, Y. Zhong, and H. Liu, Coupling theory of quasinormal modes for lossy and dispersive plasmonic nanoresonators, *Phys. Rev. B* **102**, 045430 (2020).
- [17] H. Haus and W. Huang, Coupled-mode theory, *Proc. IEEE* **79**, 1505 (1991).
- [18] F. Alpeggiani, N. Parappurath, E. Verhagen, and L. Kuipers, Quasinormal-mode expansion of the scattering matrix, *Phys. Rev. X* **7**, 021035 (2017).
- [19] C. Noguez, Surface plasmons on metal nanoparticles: The influence of shape and physical environment, *J. Phys. Chem. C* **111**, 3806 (2007).
- [20] R. L. Olmon, B. Slovick, T. W. Johnson, D. Shelton, S.-H. Oh, G. D. Boreman, and M. B. Raschke, Optical dielectric function of gold, *Phys. Rev. B* **86**, 235147 (2012).
- [21] J. Fregoni, T. S. Haugland, S. Pipolo, T. Giovannini, H. Koch, and S. Corni, Strong coupling between localized surface plasmons and molecules by coupled cluster theory, *Nano Lett.* **21**, 6664 (2021).
- [22] T. Neuman, R. Esteban, D. Casanova, F. J. García-Vidal, and J. Aizpurua, Coupling of molecular emitters and plasmonic cavities beyond the point-dipole approximation, *Nano Lett.* **18**, 2358 (2018).
- [23] E. Rephaeli and S. Fan, Few-photon single-atom cavity QED with input-output formalism in Fock space, *IEEE J. Sel. Top. Quantum Electron.* **18**, 1754 (2012).
- [24] L. Tsang and J. A. Kong, *Scattering of Electromagnetic Waves: Advanced Topics* (Wiley, New York, 2004).
- [25] M. K. Dezfouli, C. Tserkezis, N. A. Mortensen, and S. Hughes, Nonlocal quasinormal modes for arbitrarily shaped three-dimensional plasmonic resonators, *Optica* **4**, 1503 (2017).
- [26] F. Binkowski, L. Zschiedrich, M. Hammerschmidt, and S. Burger, Modal analysis for nanoplasmonics with nonlocal material properties, *Phys. Rev. B* **100**, 155406 (2019).
- [27] Q. Zhou, P. Zhang, and X.-W. Chen, General framework of canonical quasinormal mode analysis for extreme nano-optics, *Phys. Rev. Lett.* **127**, 267401 (2021).
- [28] Q. Zhou, P. Zhang, and X.-W. Chen, Quasinormal mode theory for nanoscale electromagnetism informed by quantum surface response, *Phys. Rev. B* **105**, 125419 (2022).
- [29] C. Tao, Y. Zhong, and H. Liu, Quasinormal mode expansion theory for mesoscale plasmonic nanoresonators: An analytical treatment of nonclassical electromagnetic boundary condition, *Phys. Rev. Lett.* **129**, 197401 (2022).
- [30] C. Sauvan, J. P. Hugonin, I. S. Maksymov, and P. Lalanne, Theory of the spontaneous optical emission of nanosize photonic and plasmon resonators, *Phys. Rev. Lett.* **110**, 237401 (2013).
- [31] N. Kongsuwan, A. Demetriadou, M. Horton, R. Chikkaraddy, J. J. Baumberg, and O. Hess, Plasmonic nanocavity modes: From near-field to far-field radiation, *ACS Photonics* **7**, 463 (2020).
- [32] L. Tsang, J. A. Kong, and K.-H. Ding, *Scattering of Electromagnetic Waves: Theories and Applications* (Wiley, New York, 2000), Vol. 15.
- [33] P. Lalanne, W. Yan, K. Vynck, C. Sauvan, and J.-P. Hugonin, Light interaction with photonic and plasmonic resonances, *Laser Photonics Rev.* **12**, 1700113 (2018).
- [34] M. Ida, On the relation between the phase shift and the number of bound states, *Prog. Theor. Phys.* **21**, 625 (1959).
- [35] S. B. Hasan, R. Filter, A. Ahmed, R. Vogelgesang, R. Gordon, C. Rockstuhl, and F. Lederer, Relating localized nanoparticle resonances to an associated antenna problem, *Phys. Rev. B* **84**, 195405 (2011).
- [36] R. Carminati, A. Cazé, D. Cao, F. Peragut, V. Krachmalnicoff, R. Pierrat, and Y. De Wilde, Electromagnetic density of states in complex plasmonic systems, *Surf. Sci. Rep.* **70**, 1 (2015).
- [37] B. Luk'Yanchuk, N. I. Zheludev, S. A. Maier, N. J. Halas, P. Nordlander, H. Giessen, and C. T. Chong, The Fano resonance in plasmonic nanostructures and metamaterials, *Nat. Mater.* **9**, 707 (2010).
- [38] H. T. Dung, L. Knöll, and D.-G. Welsch, Three-dimensional quantization of the electromagnetic field in dispersive and absorbing inhomogeneous dielectrics, *Phys. Rev. A* **57**, 3931 (1998).
- [39] L. Knöll, S. Scheel, and D.-G. Welsch, in *Coherence and Statistics of Photons and Atoms*, edited by J. Peřina (Wiley, New York, 2001), p. 1.
- [40] G. B. Arfken, H. J. Weber, and F. E. Harris, *Mathematical Methods for Physicists: A Comprehensive Guide* (Academic Press, New York, 2011).
- [41] Á. Rivas and S. F. Huelga, *Open Quantum Systems*, Springer Briefs in Physics Vol. 10 (Springer, Berlin, 2012).
- [42] H.-P. Breuer, E.-M. Laine, J. Piilo, and B. Vacchini, *Colloquium: Non-Markovian dynamics in open quantum systems*, *Rev. Mod. Phys.* **88**, 021002 (2016).
- [43] I. Medina, F. J. García-Vidal, A. I. Fernández-Domínguez, and J. Feist, Few-mode field quantization of arbitrary electromagnetic spectral densities, *Phys. Rev. Lett.* **126**, 093601 (2021).
- [44] T. Wu, M. Gurioli, and P. Lalanne, Nanoscale light confinement: The Q's and V's, *ACS Photonics* **8**, 1522 (2021).
- [45] Y. Yang, R. Chikkaraddy, Q. Lin, D. D. A. Clarke, D. Wigger, J. J. Baumberg, and O. Hess, Electrochemically switchable multimode strong coupling in plasmonic nanocavities, *Nano Lett.* **24**, 238 (2024).
- [46] S. Rocchetti, A. Ohmann, R. Chikkaraddy, G. Kang, U. F. Keyser, and J. J. Baumberg, Amplified plasmonic forces from DNA origami-scaffolded single dyes in nanogaps, *Nano Lett.* **23**, 5959 (2023).
- [47] A. Vagov, I. A. Larkin, M. D. Croitoru, and V. M. Axt, Role of nonlocality and Landau damping in the dynamics of a quantum dot coupled to surface plasmons, *Phys. Rev. B* **93**, 195414 (2016).

- [48] A. Vagov, I. Larkin, M. Croitoru, and V. M. Axt, Superanomalous skin-effect and enhanced absorption of light scattered on conductive media, *Sci. Rep.* **13**, 5103 (2023).
- [49] J. Khurgin, W.-Y. Tsai, D. P. Tsai, and G. Sun, Landau damping and limit to field confinement and enhancement in plasmonic dimers, *ACS Photonics* **4**, 2871 (2017).
- [50] G. T. Landi, D. Poletti, and G. Schaller, Nonequilibrium boundary-driven quantum systems: Models, methods, and properties, *Rev. Mod. Phys.* **94**, 045006 (2022).
- [51] Z. Jalali-Mola, S. Asgarnezhad-Zorgabad, and O. Hess, Collective quantum dynamics with distant quantum emitters in slow-wave nanoplasmonic waveguides, *App. Phys. Lett. Quantum* **1**, 046104 (2024).
- [52] C. J. S. Martinez, J. Feist, and F. J. García-Vidal, A mixed perturbative-nonperturbative treatment for strong light-matter interactions, *Nanophotonics* **13**, 2669 (2024).
- [53] J. Griffiths, T. Földes, B. de Nijs, R. Chikkaraddy, D. Wright, W. M. Deacon, D. Berta, C. Readman, D.-B. Grys, E. Rosta, and J. J. Baumberg, Resolving sub-angstrom ambient motion through reconstruction from vibrational spectra, *Nat. Commun.* **12**, 6759 (2021).